Journal of Multiscale Material Informatics
ISSN 3047-5724

Research Article

Thermal Conductivity Analysis of Functional Gradient Materials Based on Physics-Informed Neural Networks (PINNs)

Yong Ping Feng[1], Jinxiu Hu[1*]

[1]School of Traffic Engineering, Dalian Jiaotong University, Dalian 116028, China
*Corresponding: hujinxiu@djtu.edu.cn

Abstract

This paper investigates transient heat conduction problems in functionally graded materials (FGMs) using Physics-Informed Neural Networks (PINNs) and Augmented Lagrangian Physics-Informed Neural Networks (AL-PINNs). By constructing residual loss functions for the governing equations and boundary initial conditions, this method trains the neural network without relying on sample data, thereby enhancing the model's generalisation capability and reducing the reliance on the pre-processing tasks, such as the derivation of differential equations, complex modelling, and mesh generation, required by traditional numerical methods. This paper investigates the applicability of PINN and AL-PINN in solving transient heat conduction problems in FGMs and analyses the impact of network architecture on prediction accuracy. The results indicate that AL-PINN exhibits lower error than conventional PINN when addressing transient FGM heat conduction problems with complex boundaries. Although the training cost of PINN-based methods is still higher than that of the conventional Finite Element Method for small-scale benchmark problems, the proposed framework offers greater flexibility for problems with irregular geometries and variable material properties, without requiring mesh generation.

Keywords: Physics-Informed Neural Networks, Augmented Lagrangian Method, Functionally Graded Materials, Heat Conduction Analysis.

Received: 8 May 2026 / **Revised:** 19 June 2026 / **Accepted:** 23 June 2026 / **Published:** 3 July 2026

1. INTRODUCTION

In engineering fields such as chemical, energy, and aerospace engineering, accurate prediction of heat conduction problems is of great significance for material design, structural safety, and in-service performance. FGMs are widely used in high-temperature protective structures, thermal barrier coatings, and reaction equipment due to their spatially continuous variation in material properties, which effectively alleviates stress concentrations at interfaces and enhances the thermal stability of structures [1]. However, the spatially varying material parameters of FGMs make mathematical models for their heat-conduction problems highly non-uniform and complex, thereby increasing the difficulty of numerical solutions. Furthermore, in practical engineering applications, functionally graded materials are often subject to multiple thermal boundary conditions and complex loads, which further complicates heat conduction analysis.

Traditional numerical methods, such as the Finite Difference Method (FDM) [2], the Finite Element Method (FEM) [3], and the Boundary Element Method (BEM) [4], have achieved considerable success in solving partial differential equations for heat conduction. However, these methods typically require complex preprocessing steps, including the discretisation of governing equations, mesh generation, and numerical stability analysis. Particularly when dealing with complex geometries or highly non-uniform material parameters, the computational cost is high, and the modelling process is cumbersome [5].

In recent years, advances in computational capabilities and the development of data-driven methods have gradually introduced machine learning techniques into the field of scientific computing. Models such as Deep Neural Networks (DNNs) [6] and Convolutional Neural Networks (CNNs) [7] have demonstrated excellent capabilities for function approximation and have been successfully applied in various fields, including computational mechanics, material property modelling, and structural inspection [8]. However, traditional machine learning methods typically rely on large amounts of labelled data for training, whereas high-quality data is often difficult to obtain for engineering physics problems. Furthermore, such methods frequently fail to fully utilise known physical laws within the problem, such as governing equations and boundary conditions, resulting in inefficient use of information. In particular, for heat conduction problems

in gradient-property materials, the high cost and complex conditions associated with experimental data collection limit the practical application of purely data-driven methods.

To address this issue, Raissi et al. [9] proposed Physics-Informed Neural Networks (PINNs). This method embeds the residuals of partial differential equations, boundary conditions, and initial conditions into the neural network's loss function, enabling it to simultaneously satisfy both data constraints and physical laws during training, thereby significantly reducing reliance on large-scale labelled data. It has achieved good results in problems such as diffusion equations and fluid dynamics [10]–[12]. Subsequent research has further expanded the scope of PINN applications to multiple fields, including cardiovascular system simulation, turbulence analysis, crack quantification, and uncertainty modelling [13]–[16], and it has gradually become an important tool for data-driven scientific computing [17]–[18]. In recent years, the PINN method has also been applied to nonlinear heat conduction, transient heat transfer, and multiphysics coupling problems [19]–[21], demonstrating superior generalisation capabilities and computational efficiency compared to traditional methods. Recent studies have further extended physics-informed learning methods to transient heat conduction analysis in functionally graded materials (FGMs), demonstrating their effectiveness in handling spatially varying thermal properties and complex heat transfer processes [22], [23].

Although PINNs demonstrate strong capabilities in solving partial differential equations, they still face certain limitations when addressing complex engineering problems. When problems involve complex geometries, multiscale features, or significant variations in material properties, a single neural network often struggles to fully capture solution characteristics across the entire domain, leading to slow convergence during training or reduced prediction accuracy [24], [25]. Furthermore, in standard PINN frameworks, the weights of various loss terms (such as PDE residuals, boundary conditions, and initial conditions) are typically fixed values, lacking a dynamic adjustment mechanism, which further limits the model's performance under multi-constraint conditions [26]–[28].

To address these issues, the Augmented Lagrangian Method (ALM) has been introduced into the PINN framework [29], [30], yielding Augmented Lagrangian Physics-Informed Neural Networks (AL-PINNs). This method dynamically updates the weights of each loss term by adaptively adjusting the Lagrangian multipliers and penalty parameters during training, thereby enhancing the network's adaptability and flexibility to different physical constraints. Numerical experiments demonstrate that, when solving typical PDE problems such as the Burgers and Helmholtz equations, AL-PINN significantly improves prediction accuracy and training stability compared to existing dynamic equilibrium strategies. However, research on the application of AL-PINN to heat conduction problems in functionally graded materials, which exhibit significant spatial variations in material properties and complex geometries, remains limited. These studies did not specifically address the combined challenges posed by spatially varying thermal-conductivity gradients and complex geometric boundaries inherent in FGM heat conduction. To this end, this paper introduces the AL-PINN method into the modelling and solution of heat conduction in functionally graded materials, aiming to enhance the network's adaptability to complex material and geometric features, whilst verifying its predictive performance and robustness in practical engineering scenarios, thereby providing a new data-driven tool for high-precision heat conduction analysis.

Compared with existing studies on PINN-based heat conduction analysis, this work's novelty lies in the following aspects. First, this study extends the AL-PINN framework to transient heat conduction problems in FGMs with spatially varying thermal conductivity and complex geometric boundaries. Existing PINN studies primarily focus on homogeneous materials or on conventional heat transfer equations, whereas the present work specifically addresses the strong nonlinearity arising from material-property gradients. Second, an augmented Lagrangian strategy is introduced to dynamically balance PDE residuals and boundary/initial condition constraints during training. This improves the stability and convergence behavior of PINN when solving heat conduction problems involving irregular geometries and highly non-uniform thermal properties. Third, this work systematically investigates the effects of network depth and width on prediction accuracy and convergence efficiency for FGM heat-conduction problems. The relationship between network architecture and solution performance is quantitatively analyzed through multiple benchmark cases.

Finally, comparative analyses are conducted between PINN, AL-PINN, FEM reference solutions, and analytical solutions for both two- and three-dimensional transient heat conduction problems, providing a more comprehensive evaluation of the proposed framework.

2. BASIC THEORY

2.1 Problem Definition

Consider a two-dimensional or three-dimensional bounded domain Ω ($\Omega \subseteq \mathbb{R}^d$, d=2,3), with boundaries $\Gamma = \partial\Omega$. Suppose the thermal properties of the FGM vary with spatial position, i.e. the thermal conductivity $k(x)$ is a function of the coordinates. The transient heat conduction control equation with an internal heat source can then be expressed as:

$$\nabla(k(x)\nabla T(x,t)) + Q(x,t) = \rho c \frac{\partial T(x,t)}{\partial t}, (x \in \Omega, t > 0) \tag{1}$$

To determine the unique solution for the temperature field, boundary conditions and initial conditions must be specified:

$$\begin{cases} T(x,t) = \bar{T}(x,t) & (x \in \Gamma_1) \\ -k(x)\dfrac{\partial T}{\partial n} = \bar{q}(x,t) & (x \in \Gamma_2) \\ T(x,0) = T_0(x) & (x \in \Omega) \end{cases} \tag{2}$$

Where x is the spatial position coordinate vector; in two-dimensional problems, $\boldsymbol{x}=(x,y)$, and in three-dimensional problems, $\boldsymbol{x}=(x,y,z)$; t is time; $T(x,t)$ is the temperature field distribution to be solved; $k(x)$ is the thermal conductivity varying with spatial position; ρ and c are the material's density and specific heat capacity, respectively; $Q(x,t)$ is the internal heat source term.

For functionally graded materials, the thermal conductivity is spatially dependent and varies continuously with the coordinate position. Therefore, the transient heat conduction equation contains variable-coefficient diffusion terms. In the present study, the divergence term is expressed as:

$$\nabla(k(x)\nabla T) = k(x)\nabla^2 T + \nabla k(x)\nabla T \tag{3}$$

where $\nabla k(x)$ represents the spatial gradient of thermal conductivity. This term characterizes the influence of material property variation on heat flux redistribution and is automatically evaluated through automatic differentiation within the PINN framework. During training, the residual PDE loss is constructed using the complete variable-coefficient governing equation rather than assuming constant thermal conductivity.

In the current implementation, the spatial gradient $\nabla k(x)$ is analytically evaluated when the thermal conductivity is expressed in closed form (e.g., linear or polynomial distributions). The complete variable-coefficient PDE residual is then assembled and evaluated at collocation points through PyTorch's automatic differentiation engine, which computes all required partial derivatives of the network output with respect to spatial and temporal inputs.

2.2 Basic Principles of PINN for Solving Heat Conduction Problems

The core concept of PINNs is to embed the heat conduction equation and its boundary conditions as physical constraints directly into the loss function of a deep learning model. As shown in Figure 1, the training process of a PINN model essentially involves using optimisation algorithms to find the optimal network parameters $[\theta^*] = \arg min_\theta \{\mathrm{L}(\theta)\}$. The total loss function $\mathrm{L}(\theta)$ consists of a weighted sum of three components: the residual loss of the governing equation, the initial condition loss, and the boundary condition loss:

$$\mathrm{L}(\theta) = \lambda_f \mathrm{L}_f^{\mathrm{T}}(\theta) + \lambda_{ic} \mathrm{L}_{ic}^{\mathrm{T}}(\theta) + \lambda_{bc} \mathrm{L}_{bc}^{\mathrm{T}}(\theta) \tag{4}$$

where $\lambda_{\mathbf{f}}$, $\lambda_{\mathbf{ic}}$ and λ_{bc} denote the penalty weight coefficients for each loss term, respectively. Specifically, the initial condition loss term $\mathrm{L}_{ic}^{\mathrm{T}}(\theta)$ and the boundary condition loss term $\mathrm{L}_{bc}^{\mathrm{T}}(\theta)$ are used to constrain the network's output to approximate the true physical field at the initial time t_{ic} and at the spatio-temporal boundary (x_{bc},t_{bc}), respectively.

Initial condition loss:

$$\text{loss}: \frac{1}{N_{ic}} \sum_{j=1}^{N_{ic}} \left| \mathrm{T}_\theta(x_{ic}^j, t_{ic}^j) - \mathrm{G}_\Gamma(x_{ic}^j, t_{ic}^j) \right|^2 \tag{5}$$

Boundary condition loss:

$$\text{loss}: \frac{1}{N_{bc}} \sum_{m=1}^{N_{bc}} \left| T_\theta(x_{bc}^m, t_{bc}^m) - \mathrm{H}_\Gamma(x_{bc}^m, t_{bc}^m) \right|^2 \tag{6}$$

where N_{ic} and N_{bc} denote the respective numbers of collocation points, and G_Γ and H_Γ represent the given initial and boundary condition distributions. As the core physical constraint of the PINN architecture, the residual loss term for the governing equations $\mathrm{L}_f^{\mathrm{T}}(\theta)$ calculates the residuals for transient heat conduction energy conservation across F_f randomly sampled collocation points (x_f,t_f) within the solution domain.

$$\mathrm{L}_f^{\mathrm{T}}(\theta) = \frac{1}{N_f} \sum_{k=1}^{N_f} \left| \rho c \dot{T}_\theta(x_f^k, t_f^k) + q_{i,i}(x_f^k, t_f^k) - Q_i(x_f^k, t_f^k) \right|^2 \tag{7}$$

where ρ is the density, c is the specific heat capacity, Q_i is the internal heat source term, $\dot{T}_\theta$ is the derivative of the network-predicted temperature with respect to time, and $q_{i,i}$ is the divergence term of the heat flux density.

In the calculation of the aforementioned physical residuals, PINN uses a deep neural network (DNN) as the underlying approximator, which takes spatiotemporal coordinates (x, t) as input and outputs the predicted temperature $T_\theta(x,t)$. Unlike traditional numerical methods that rely on grid discretisation, PINN uses Automatic Differentiation (AD). Upon completion of training, to quantify the model's prediction accuracy for transient temperature fields, the Mean Relative Error (MRE) is typically introduced as a global evaluation metric, supplemented by the Maximum Relative Error (Max-RE) to measure local maximum deviations. The expression for MRE is:

$$\mathrm{MRE}=\frac{1}{N_t}\sum_{i=1}^{N_t}\frac{|T_{pred}(x_t^i,t_t^i)-T_{exact}(x_t^i,t_t^i)|}{|T_{exact}(x_t^i,t_t^i)|} \tag{8}$$

where T_{pred} is the predicted temperature by the PINN on the test set, T_{exact} is the reference solution (analytical solution or high-precision numerical solution), and N_t is the total number of test data points.

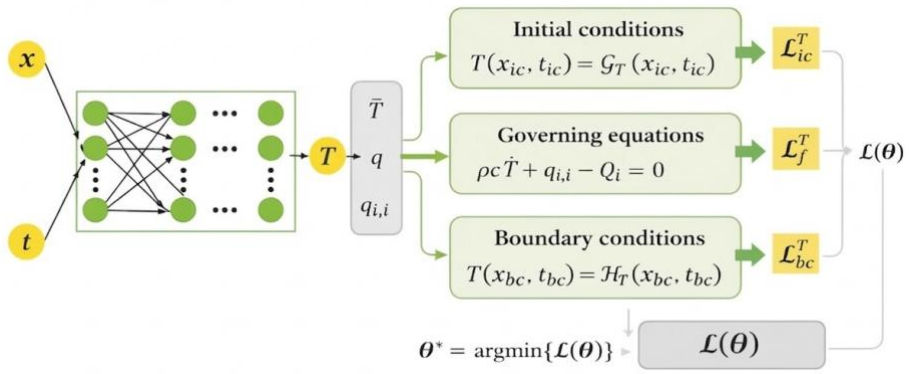

Figure 1. Diagram of PINN for heat conduction problems.

2.3 Basic Principles of the AL-PINN for Solving Heat Conduction Problems

When applying PINN to solve transient heat conduction problems in functionally graded materials, the loss function is typically constituted by a weighted sum of the residuals of the governing equations (PDE Loss), boundary conditions (BC Loss) and initial conditions (IC Loss). However, due to significant differences in the statistical properties of the gradients of PDE residuals and boundary/initial condition residuals, traditional fixed-weight summation methods often make it difficult for the network to balance the various constraints during training, leading to local optima or significant errors at the boundaries.

To address this optimisation challenge, this paper adopts the AL-PINN method proposed by Son et al [31]. Rather than simply incorporating boundary and initial conditions as soft constraints into the loss function, this method treats them as hard constraints in a constrained optimisation problem and transforms it into an unconstrained Min-Max optimisation problem using the augmented Lagrangian multiplier method.

2.3.1 Formulation of the Constrained Optimisation Problem

For the FGM transient heat conduction problem defined in Section 2.1, we model the process of finding the neural network parameters $\boldsymbol{\theta}$ as the following constrained optimisation problem:

$$\begin{aligned}&\min_{\boldsymbol{\theta}} \mathrm{J}_{PDE}(\boldsymbol{\theta})=\frac{1}{N_f}\sum_{k=1}^{N_f}\|f(\boldsymbol{x}_f^k,t_f^k;\boldsymbol{\theta})\|^2\\ &\text{s.t.}\quad\begin{cases}T(\boldsymbol{x},t;\boldsymbol{\theta})-\bar{T}(\boldsymbol{x},t)=0, & (\boldsymbol{x},t)\in\Gamma_1\times[0,\mathrm{T}]\\ -k(\boldsymbol{x})\dfrac{\partial T}{\partial n}-\bar{q}(\boldsymbol{x},t)=0, & (\boldsymbol{x},t)\in\Gamma_2\times[0,\mathrm{T}]\\ T(\boldsymbol{x},0;\boldsymbol{\theta})-T_0(\boldsymbol{x})=0, & \boldsymbol{x}\in\Omega\end{cases}\end{aligned} \tag{9}$$

where f represents the residual of the control equation defined in Equation (9); that is, the objective function comprises only the mean squared error of the physical equations, whilst all boundary and initial conditions are treated as equality constraints $C(\boldsymbol{\theta})=0$.

2.3.2 Augmented Lagrangian loss function

Based on the Method of Multipliers, the above constrained optimisation problem is transformed into finding the saddle point of the augmented Lagrangian function $\mathrm{L}(\boldsymbol{\theta},\boldsymbol{\lambda})$. For FGMs heat conduction problems, the total loss function of AL-PINN is defined as:

$$L(\theta,\lambda) = J_{PDE}(\theta) + \sum_{i\in\{bc1,bc2,ic\}} (\frac{\beta}{2} J_i(\theta) + \langle \lambda_i, r_i(\theta)\rangle) \tag{10}$$

Expanding this in detail:

$$\begin{aligned} &\frac{1}{N_f}\sum \| f\|^2 \quad + \frac{\beta}{2N_{b1}}\sum \| T-\bar{T}\|^2 + \frac{1}{N_{b1}}\sum \lambda_{b1}^{(j)}(T-\bar{T}) \quad + \\ &\frac{\beta}{2N_{b2}}\sum \left\| -k\frac{\partial T}{\partial n} - \bar{q}\right\|^2 + \frac{1}{N_{b2}}\sum \lambda_{b2}^{(j)}\left(-k\frac{\partial T}{\partial n} - \bar{q}\right) \quad + \\ &\frac{\beta}{2N_{ic}}\sum \| T-T_0\|^2 + \frac{1}{N_{ic}}\sum \lambda_{ic}^{(j)}(T-T_0) \end{aligned} \tag{11}$$

where $\beta > 0$ is the penalty parameter, used to ensure the convexity and numerical stability of the algorithm; $\boldsymbol{\lambda}_{b1}, \boldsymbol{\lambda}_{b2}, \boldsymbol{\lambda}_{ic}$ are the Lagrange multipliers corresponding to the first-class boundary, second-class boundary and initial conditions, respectively. Unlike the scalar weights in traditional PINNs, here there is a vector that corresponds one-to-one to the sampling points; that is, each boundary/initial sampling point has an independent, learnable weight.

2.3.3 Training Algorithm

The training process of AL-PINN is a Min-Max game, aiming to find parameters $\boldsymbol{\theta}$ that minimise the loss function whilst simultaneously finding multipliers $\boldsymbol{\lambda}$ that maximise the loss function (to satisfy the constraints). The training process employs an alternating update strategy: (1) Update the network parameters $\boldsymbol{\theta}$ (minimisation step): Fix the Lagrange multiplier $\boldsymbol{\lambda}$ and use stochastic gradient descent (SGD) or the Adam optimiser to update the neural network weights, thereby minimising L：

$$\boldsymbol{\theta}^{k+1} \leftarrow \boldsymbol{\theta}^k - \eta_\theta \nabla_\theta \mathrm{L}(\boldsymbol{\theta}^k, \boldsymbol{\lambda}^k) \tag{12}$$

(2) Update the Lagrangian multiplier $\boldsymbol{\lambda}$ (maximisation step): Fix the network parameters $\boldsymbol{\theta}$ and update the multiplier $\boldsymbol{\lambda}$ in the direction of the gradient, forcing the network to better satisfy the boundary and initial condition constraints:

$$\boldsymbol{\lambda}^{k+1} \leftarrow \boldsymbol{\lambda}^k + \eta_\lambda \nabla_\lambda \mathrm{L}(\boldsymbol{\theta}^{k+1}, \boldsymbol{\lambda}^k) \tag{13}$$

According to Equation (14), the update of the multipliers is effectively the accumulation of the current residual:

$$\boldsymbol{\lambda}^{k+1} = \boldsymbol{\lambda}^k + \eta_\lambda \boldsymbol{r}(\boldsymbol{\theta}^{k+1}) \tag{14}$$

Through this adaptive adjustment mechanism, AL-PINN automatically allocates weights to different regions during training. In the early stages of training or in boundary regions with high error rates, the Lagrange multiplier $\boldsymbol{\lambda}$ automatically increases, thereby forcing the network to prioritise learning these 'difficult' samples. As shown in Figure 2, compared to traditional PINNs, AL-PINNs achieve higher accuracy and faster convergence when solving heat conduction problems for FGMs with complex boundary conditions and regions of drastic material property changes.

The multiplier update mechanism can be interpreted as an adaptive weighting strategy for physical constraints. During training, if the residuals associated with boundary or initial conditions remain large, the corresponding Lagrange multipliers automatically increase. Consequently, the optimization process allocates more attention to regions with large physical inconsistencies. Compared with conventional PINNs using fixed weighting coefficients, AL-PINN dynamically balances PDE residual minimization and boundary condition enforcement, thereby improving convergence stability and reducing local error accumulation near complex boundaries. In this study, the penalty parameter β was initialized as a small positive constant and progressively increased during training. This strategy improves numerical stability during the early training stage while enforcing stricter physical constraints during later optimization stages. Figure 2 illustrates the alternating optimization strategy of AL-PINN. The neural network parameters are first updated to minimize the augmented Lagrangian loss, followed by updates to the Lagrange multipliers to strengthen constraint enforcement. This iterative min-max optimization process enables adaptive balancing among different physical constraints. The penalty parameter β was initialized to 1 and doubled every 10,000 iterations up to a maximum value of 100. The Lagrange multiplier learning rate was set to $\eta_\lambda = 0.01$, and multipliers were updated every 1,000 iterations following the network parameter update step.

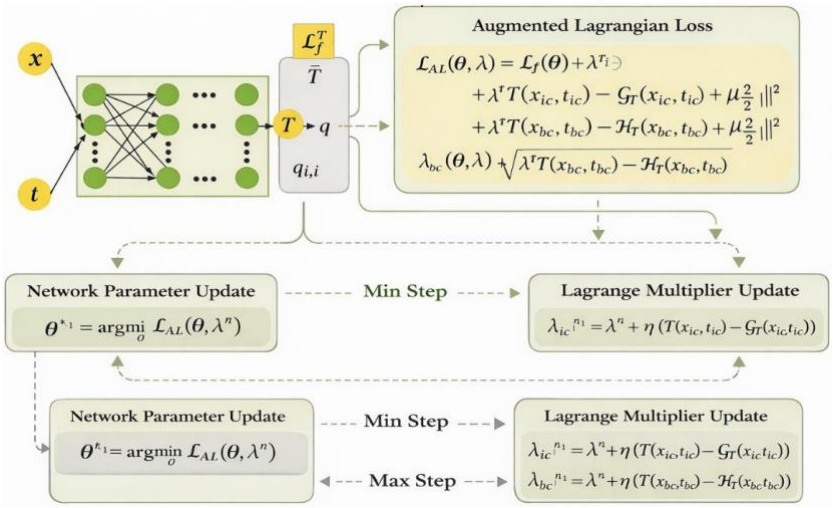

Figure 2. Diagram of AL- PINN for heat conduction problems.

2.4 Network Architecture and Training Configuration

The neural network adopted in this study is a fully connected feed-forward neural network with Tanh activation functions. The input variables consist of spatial coordinates and time, while the output variable corresponds to the predicted temperature field. The Adam optimizer was employed during training with an initial learning rate of 1×10^{-3}. The learning rate was gradually reduced during optimization using a step decay strategy. Xavier initialization was adopted for all trainable parameters. To investigate the influence of network architecture, different combinations of hidden layers (2, 4, 6, and 8) and neuron counts per layer (128 and 256) were systematically tested. The collocation points inside the domain and on the boundaries were generated using Latin Hypercube Sampling (LHS) to improve spatial coverage and sampling uniformity. The stopping criterion was either reaching 60,000 training iterations or achieving stable convergence of the total loss. The batch size for collocation points was fixed during training. The learning rate decay factor was set to 0.5 every 10,000 iterations to improve optimization stability during later training stages. The selected network depth and width combinations were chosen to balance nonlinear representation capability and computational cost based on preliminary numerical experiments. A sensitivity study of the number of collocation points was conducted for Case Study 1, and the selected values provided sufficient spatial coverage while maintaining acceptable computational cost. The above training configurations were uniformly applied across all three benchmark cases unless otherwise stated.

3. NUMERICAL EXAMPLES

3.1 Case Study 1

To verify the validity and accuracy of the numerical method proposed in this paper, a heat conduction case study was constructed for analysis. The geometric model, shown in Figure 3, consists of a rectangular plate with length L = 0.2 m and width W = 0.1 m, with a circular hole of radius r = 0.025 m located at its centre. The thermal properties of the material are set as follows: density ρ = 2700 kg/m³, specific heat capacity c = 996 J/(kg·°C); taking into account the inhomogeneity of the medium, the thermal conductivity is set as a function $k(x)$ = 150 + 500xW/(m·°C) that varies linearly with the x-coordinate.

The initial temperature field in the solution domain is set to a uniform distribution T_0 = 0 °C. For the boundary conditions at $t > 0$, adiabatic boundary conditions ($\partial T/\partial t = 0$) are applied to the upper and lower surfaces of the rectangular plate and the inner wall of the circular hole; the right boundary ($x = L$) is maintained at a constant temperature T = 0 °C; the left boundary (x = 0) is subjected to a time-varying periodic Dirichlet temperature load $T(0,y,t) = 100[1-\cos(\omega t)]$ °C, where the angular frequency $\omega = \pi/200$ rad/s. The finite element discretisation model is shown in Figure 4. The solution domain is divided into 2,724 quadrilateral linear elements, with a time step of $\Delta t = 1$ s.

To investigate the influence of network architecture on prediction accuracy and to verify the algorithm's generalisation capability mentioned in the abstract, this paper conducts a systematic comparative analysis of eight PINN network architectures with varying numbers of hidden layers (l = 2, 4, 6, 8) and neurons per layer (d = 128, 256). Combined with the loss function curve plots from network training, it can be observed that the eight network architectures employing the Tanh activation function all achieved good convergence within the set 60,000 training iterations, with the loss value decreasing steadily; this demonstrates the computational stability of the algorithm when solving partial differential equations with variable coefficients. The specific convergence process for each architecture is illustrated in Figure 5.

However, variations in the network's depth and width significantly affected final prediction accuracy and computational efficiency (training time).

The quantitative error analysis data in Table 2 further reveal the network architecture's optimisation patterns. When the network scale is small (e. g. l=2, d=128), the model's non-linear representation capacity is limited, with a Mean Relative Error (MRE) of 1. 4821%, With an appropriate increase in network depth, prediction accuracy improves markedly; however, when the network becomes excessively deep (e. g. l=6 or l=8), the error actually rises again (for instance, when l=8 and d=256, the MRE increases to 1.0053%). This may be due to excessively deep networks encountering optimisation difficulties or becoming trapped in local optima during non-convex optimisation. A comprehensive comparison of the various metrics indicates that a network architecture comprising 4 hidden layers, each with 256 neurons (4×256), performs best. Under this optimal configuration, the model's mean relative error (MRE) drops to an extremely low 0.0713%, the maximum relative error (Max-RE) is only 0.3599%, and the training time (5672 s) is moderate, achieving a balance between accuracy and efficiency.

Based on this optimal network structure (4×256), the comparison of the full temperature fields at t=200 clearly shows. 0s and t=400. 0s in Figure 6 that the model accurately captures the complex physical phenomena during the transient heat conduction process. In terms of spatial distribution, the temperature gradient exhibits a distinct deflection near the adiabatic boundary of the central circular aperture; in terms of temporal evolution, the periodic temperature load at the left boundary (Dirichlet boundary) triggers a dynamic shift in the temperature gradient across the entire domain. The PINN model's prediction contour plots are virtually indistinguishable from the FEM reference solution in terms of visual detail.

This case study fully validates the algorithm's accuracy in addressing transient heat-conduction problems with varying coefficients. By constructing a residual loss function for the governing equations and boundary/initial conditions, and training the neural network without relying on external sample data, the model's generalisation capability is enhanced, whilst reducing the dependence on mesh generation, the cumbersome pre-processing tasks, such as complex modelling, derivation of differential equations, and those required by traditional numerical methods (e. g., FEM). This provides an alternative, physics-constrained computational approach to solving complex multi-physics coupling and material-inclusion problems under extreme conditions.

3.1.1 Quantitative Comparison with FEM

To further evaluate the effectiveness of the proposed framework, quantitative comparisons between FEM and PINN were conducted on prediction accuracy, computational efficiency, and modeling flexibility. For the present benchmark problem, the FEM model employed 2,724 quadrilateral elements with a time step size of 1 s. Under the optimal network configuration (4×256), the PINN achieved an MRE of 0.0713%. Although FEM still exhibits higher computational efficiency for relatively small-scale benchmark problems due to its mature discretization framework, the proposed PINN-based framework eliminates the need for mesh generation and governing equation discretization. This advantage becomes increasingly important for problems involving irregular geometries, moving boundaries, and multi-physics coupling. Unlike conventional FEM, the proposed framework directly incorporates governing equations and boundary conditions into the neural network through automatic differentiation, thereby reducing the dependence on mesh quality and remeshing procedures. The comparison results demonstrate that PINN achieves competitive accuracy while offering greater flexibility for solving transient heat-conduction problems in functionally graded materials. Table 1 summarizes the comparison results between FEM and PINN.

Table1. Quantitative comparison of accuracy and computational characteristics between FEM and PINN.

Method	Mesh Required	Governing Equation Discretization	MRE (%)	Boundary Flexibility
FEM	Yes	Required	Reference (-)	Medium
PINN	No	Not Required	0. 0713	High

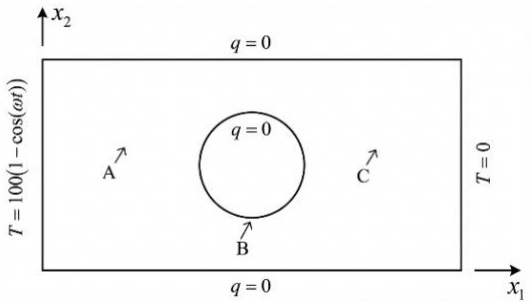

Figure 3. Geometric configuration of a rectangular plate with a circular hole.

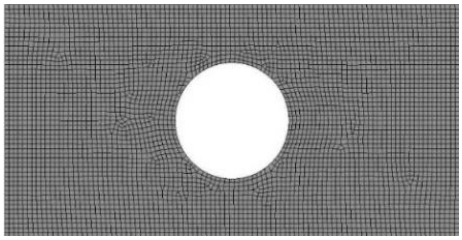

Figure 4. Finite element model of a rectangular plate with a circular hole.

Table 2. Training results for different neural network architectures.

Hidden Layers (*l*)	Neurons/Layer (*d*)	MRE/%	Max-RE/%	Training Time (s)	Iterations
2	128	1. 4821	1. 8385	2573	60,000
2	256	0. 8052	1. 5245	3,290	60,000
4	128	0. 4958	1. 3928	3,744	60,000
4	256	0. 0713	0. 3599	5,672	60,000
6	128	0. 8522	1. 1721	5,074	60,000
6	256	0. 9960	1. 8196	8,040	60,000
8	128	0. 8132	1. 8061	6,394	60,000
8	256	1. 0053	1. 9843	10,723	60,000

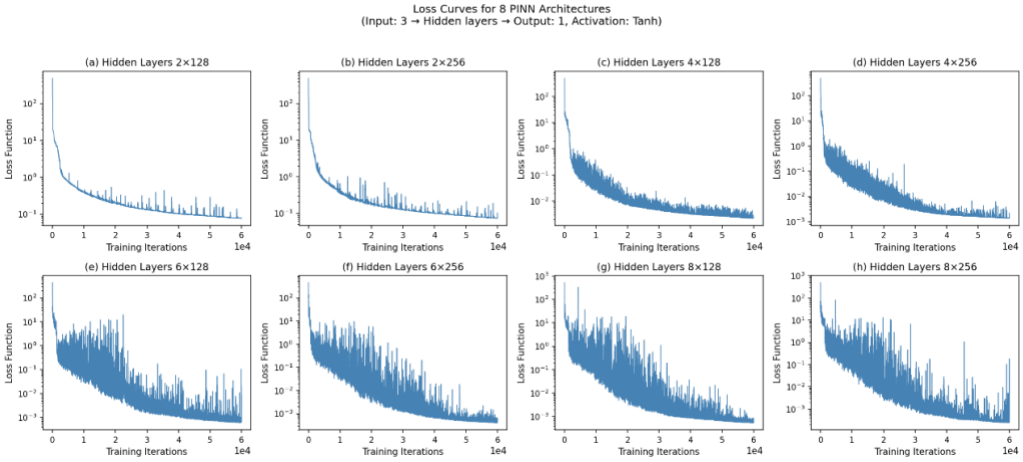

Figure 5. Convergence curve under the different network architectures.

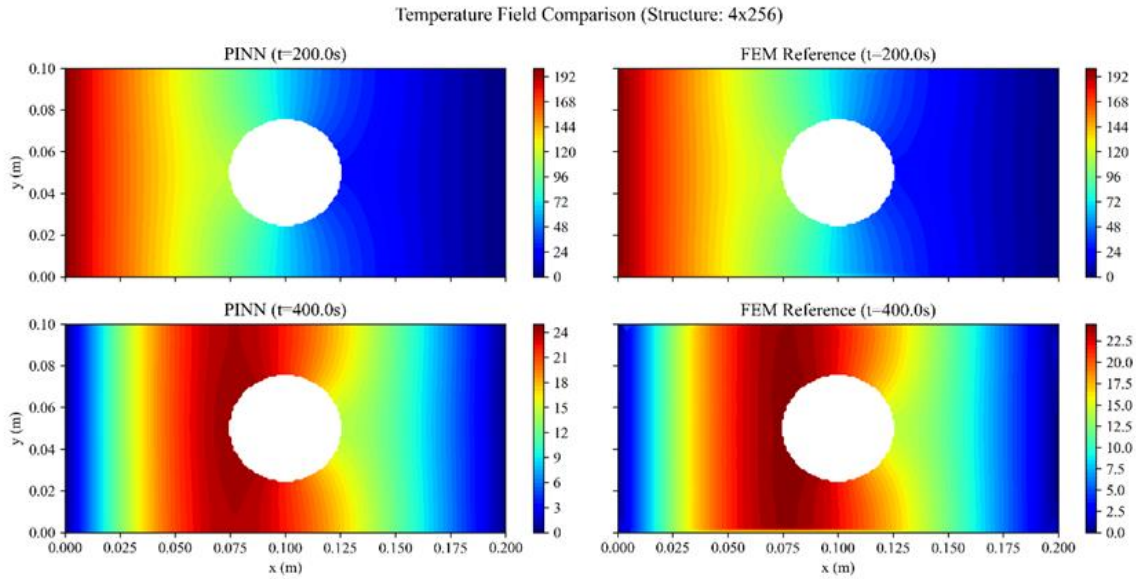

Figure 6. Comparison of temperature field contours predicted by PINN and FEM at t = 200s and t = 400s under the optimal network architecture (4×256).

3.2 Case Study 2

Consider a two-dimensional approximate model of a car wheel hub, as shown in Figure 7. Assume that the rim of the wheel hub is subject to temperature boundary conditions, whilst the rim and the junction between the axle and the wheel hub are subject to heat flux boundary conditions. The expressions for the temperature $\bar{T}(r,t)$ and heat flux $\bar{q}(r,t)$ as a function of time are:

$$\bar{T}(r,t)=\frac{r^2}{100}t+100 \quad (r\in\Gamma_1) \tag{15}$$

$$\bar{q}(r,t)=\frac{r^3}{5000}t+\frac{r}{5}t \quad (r\in\Gamma_2) \tag{16}$$

In the equations, $r=\sqrt{x^2+y^2}$ is the distance from a point on the rim to the centre of the rim. It is assumed that the thermal conductivity of the rim varies with radius, given by:

$$k(r)=\frac{r^2}{100}+10 \tag{17}$$

For the sake of simplicity, assume that the density and specific heat of the hub are constant and that $\rho=c=1$ the hub contains a heat source that varies with time, expressed as:

$$Q(r,t)=\frac{r^2}{100}-\frac{r^2}{1250}t-0.4t \tag{18}$$

The exact solution for the temperature distribution throughout the hub is:

$$T_{exact}=\left(\frac{r^2}{100}\right)t+100 \tag{19}$$

The PINN model is employed to predict the time-varying temperature field of the wheel rim. To this end, heat flux points were applied at 10 time steps (t=0. 1, 0. 2, 0. 3,…,1) along the inner and outer boundaries of the wheel rim, along with 5,682 sample points at the heat flux boundaries and 9,641 sample points within the domain. The temperature prediction results and relative errors are shown in Figure 7.

Due to the temperature boundary condition acting on the outer edge of the hub, the inner edge of the hub and the spoke connection points being constrained by the heat flux boundary condition $\tilde{q}(r,t)$, and the material's thermal conductivity $k(r)$ exhibiting a non-linear quadratic distribution with respect to the radius, as well as the inclusion of a time-varying internal heat source $\mathrm{Q(r,t)}$, this significantly increases the difficulty of solving the physical equations. Consequently, the AL-PINN model was introduced for the solution. The temperature prediction results and relative errors are shown in Figure 8. The results indicate that both the PINN and AL-PINN models can accurately capture the physical evolution of heat conduction from the outer edge towards the centre; however, they exhibit significant differences in the accuracy of constraints on complex geometric boundaries. By comparing the relative error 8 distributions at three typical time steps (t=0.1s,0.5s,1.0s) in Figure 8, it can be observed that the traditional PINN exhibits a distinct clustering of errors when handling irregular hole edges, with the maximum relative error reaching0.5181% at t=0.1s; whereas AL-PINN, through the dynamic enhancement of boundary condition residuals via the augmented Lagrangian term, reduces the average relative error at the same time step to 0.0051% , representing an improvement in accuracy of nearly two orders of magnitude.

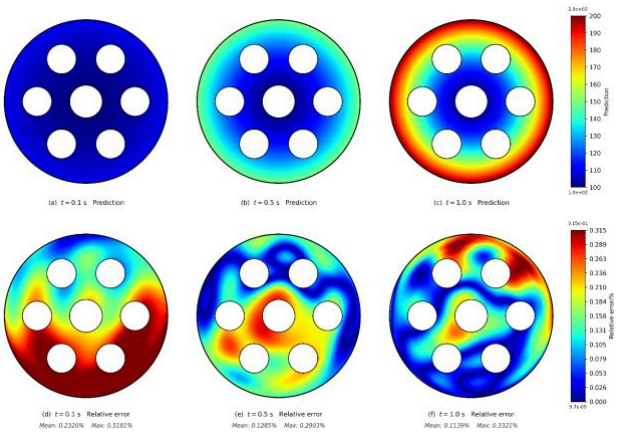

Figure 7. Temperature prediction contours and relative error distributions of conventional PINN at different transient time steps for the wheel hub benchmark problem.

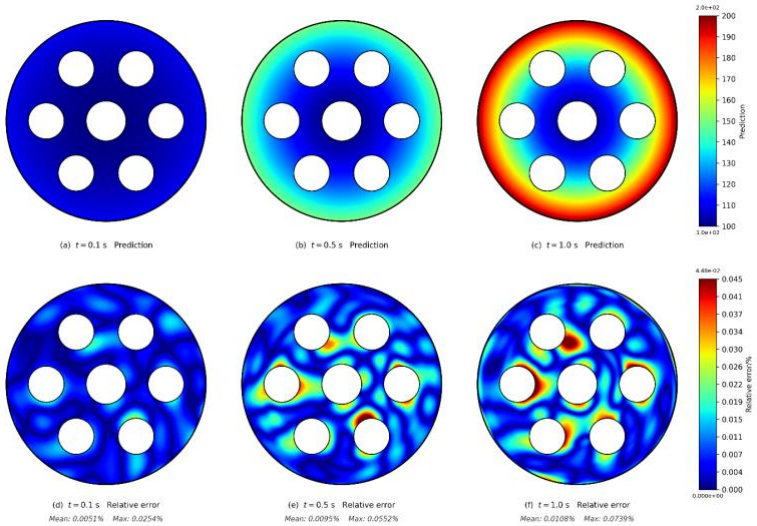

Figure 8. Temperature prediction contours and relative error distributions of AL-PINN at different transient time steps for the wheel hub benchmark problem.

In terms of training stability, the total loss, PDE residual, and initial/boundary condition loss curves of AL-PINN in Figure 9 demonstrate good convergence within 60,000 iterations. However, upon reaching approximately 20,000 iterations, as the Lagrangian multiplier and penalty parameters were updated, all component losses and prediction errors exhibited a significant step-like decrease, indicating that AL-PINN is more effective at escaping local optima. A comparison of convergence trajectories across the entire time domain is shown in Figure 10. further confirms that the mean and maximum relative errors of AL-PINN (solid line) remain at extremely low levels, demonstrating greater robustness and generalisation capability than the PINN model (dashed line). In addition to the numerical error metrics (MRE and Max-RE), the physical consistency of the predicted temperature fields was further examined through heat-flux validation. The radial heat flux recovered from the AL-PINN-predicted temperature gradients was compared with the analytical heat-flux solution derived from Fourier's law. As shown in the figure. 11, the AL-PINN heat-flux distribution follows the same spatial evolution trend as the analytical solution under variable thermal conductivity. With increasing radial position, the thermal conductivity increases, and the magnitude of the heat flux increases accordingly, consistent with the governing heat-conduction physics. The close agreement between the predicted and analytical heat-flux profiles indicates that the proposed AL-PINN framework captures not only the temperature field but also its physically meaningful gradients. Moreover, no obvious non-physical oscillations or discontinuities are observed in the predicted heat-flux distribution, further confirming the solution's physical reliability.

This case study fully demonstrates that the AL-PINN framework, when addressing transient heat conduction problems involving complex geometries and time-varying, non-uniform material properties, not only reduces the dependence on complex mesh generation procedures required by traditional finite element methods but also improves solution accuracy under complex boundary conditions through the adaptive adjustment of physical constraint weights, thereby providing robust support for the precise thermal design of engineering structures in complex environments.

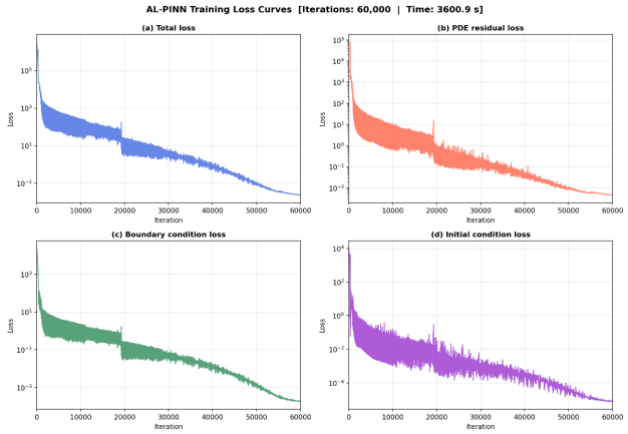

Figure 9. Training loss curves of AL-PINN, showing the decay of total loss, PDE residual loss, boundary condition loss, initial condition loss, and Lagrange multiplier regularization term over training iterations.

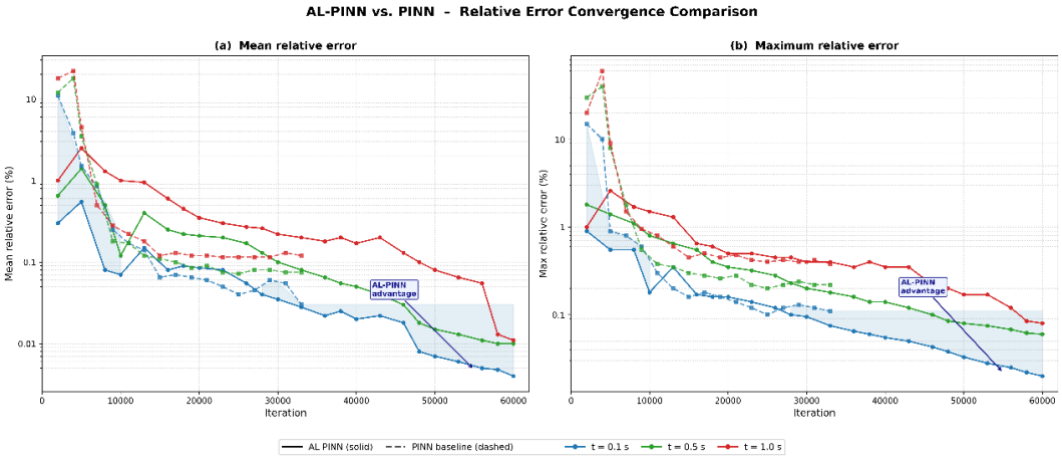

Figure 10. Convergence comparison of mean relative error and maximum relative error between PINN and AL-PINN during training iterations.

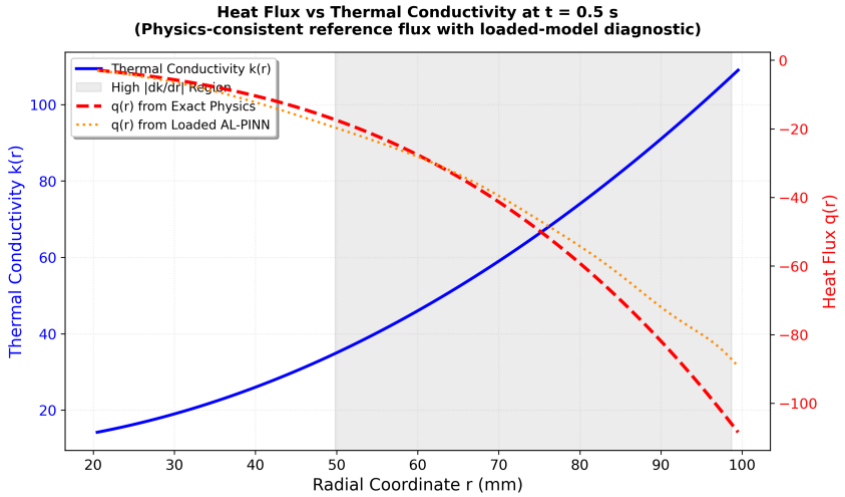

Figure 11. Comparison of analytical and AL-PINN heat-flux distributions under variable thermal conductivity ($t = 0.5$ s).

3.3 Case Study 3

Within a unit cube, the material properties vary only in the z-direction, and the boundary conditions are as follows:

$$T(x,y,1,t)=100^{\circ}C, T(x,y,0,t)=0^{\circ}C \tag{20}$$

$$q(1,y,z,t)=0, q(0,y,z,t)=0 \tag{21}$$

$$q(x,1,z,t)=0, q(x,0,z,t)=0 \tag{22}$$

and the initial conditions:

$$T(x,y,z,0)=0 \tag{23}$$

The thermal conductivity and specific heat are

$$k(x,y,z)=5e^{3z} \tag{24}$$

$$c(x,y,z)=e^{3z} \tag{25}$$

The analytical solution to this problem is expressed as follows:

$$T(x,y,z,t)=T\frac{1-e^{-2\beta z}}{1-e^{-2\beta L}}+\sum_{n=1}^{\infty}B_n\sin\left(\frac{n\pi z}{L}\right)e^{-\beta z^2}e^{-\left(\frac{n^2\pi^2}{L^2+\beta^2}\right)\alpha t} \tag{26}$$

$$B_n=\frac{-2Te^{\beta L}}{\beta^2L^2+n^2\pi^2}\left[\beta L\sin n\pi\frac{1+e^{-2\beta L}}{1-e^{-2\beta L}}-n\pi\cos n\pi\right] \tag{27}$$

where $L = 1$ is the length of the cube in the z-direction $\alpha=5, \beta=1.5, T=100$ ℃.

A total of 37,665 nodes are distributed regularly along the space-time boundary (15,795) and within the space-time domain (21,870). The distribution of spatial nodes is shown in Figure 12. During the pre-processing stage of the mesh generation, the space-time domain and boundary are discretised and sampled. These nodes will be used directly to compute the physics-informed loss function.

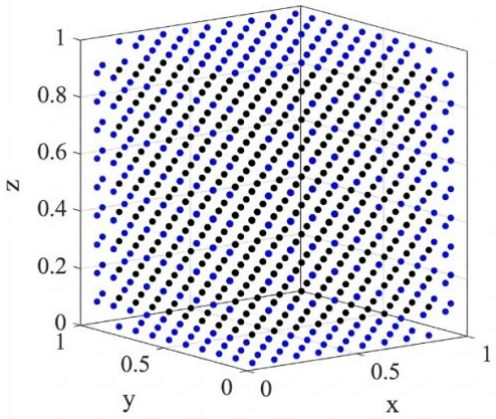

Figure 12. Node distribution diagram of collocation points and boundary points in the computational domain.

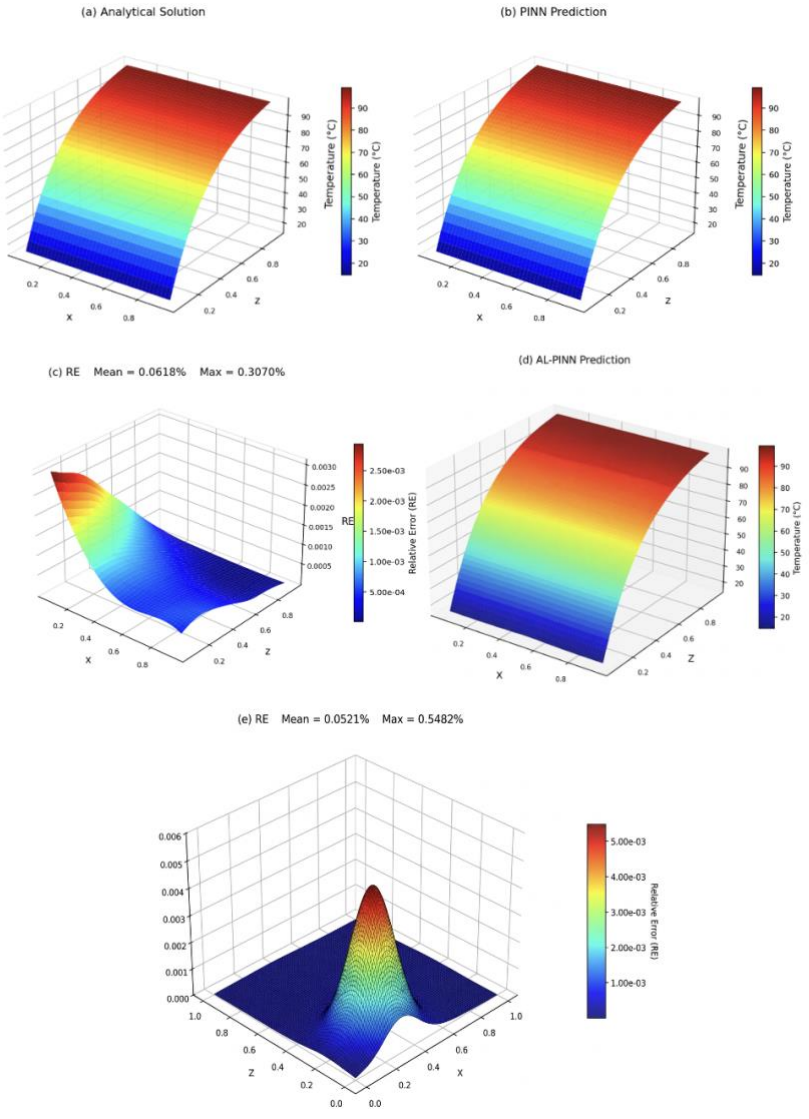

Figure 13. Contours of predicted temperature fields and corresponding relative errors obtained by PINN and AL-PINN.

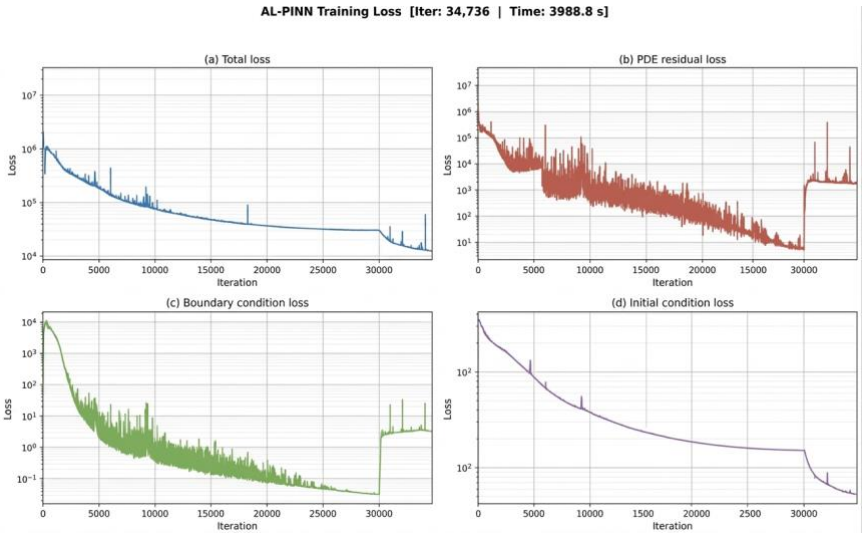

Figure 14. Training loss curves of AL-PINN, showing the decay of total loss, PDE residual loss, boundary condition loss, initial condition loss, and Lagrange multiplier regularization term over training iterations.

Upon completion of model training, we conducted a comparative analysis of the predicted temperature fields from the traditional PINN and AL-PINN against the analytical solution, as shown in Figure 13. As shown in the three-dimensional contour plots of the temperature distribution, although the traditional PINN prediction results (Figure 13b) generally align with the analytical solution (Figure 13a), there are local deviations. Furthermore, the relative error (Figure 13c) plot reveals that the traditional PINN has a mean relative error (Mean RE) of 0. 1683% and a maximum relative error (Max RE) of 0. 7869%. The errors are primarily concentrated in regions where the boundary gradients change more abruptly.

In contrast, the AL-PINN method demonstrates a significant improvement in accuracy. The temperature field prediction results from the AL-PINN (Figure d) are in high agreement with the analytical solution. Its relative error distribution plot (Figure13e) shows that the mean relative error of AL-PINN has dropped significantly to 0.0521%, whilst the maximum relative error has fallen to 0.5482%. Compared to the traditional PINN, the average error of AL-PINN has been reduced by nearly 69%. This indicates that the introduction of the augmented Lagrangian method effectively balances the weights between the residuals of the partial differential equation and those of the boundary/initial conditions, forcing the neural network to satisfy the physical constraints more strictly.

To gain a deeper understanding of the AL-PINN optimisation process, this paper presents the loss function descent curve during training in Figure 14. The model was trained for approximately 34,736 iterations, taking 3,988.8 seconds. As shown in the figure, the loss function is divided into four components: total loss, PDE residual loss, boundary condition loss, and initial condition loss. Initial convergence phase (0–30,000 steps): Under the influence of the adaptive optimiser, each loss component exhibits a steady logarithmic decline, indicating that the network has initially learnt the global patterns of heat conduction. Augmented Lagrangian Multiplier update phase (after 30,000 steps): When the number of iterations reached approximately 30,000, the curves for the total loss, PDE loss and boundary condition loss all exhibited a distinct ‘spike’. This was due to the AL-PINN algorithm triggering the dynamic update mechanism for the Lagrangian multipliers and penalty parameters. When the optimisation becomes stuck in a local minimum, or the descent of a particular loss term stagnates, the algorithm breaks the deadlock by increasing the penalty for violations of physical constraints (particularly high-gradient PDE constraints). Final convergence stage: Following the parameter update, the network continues to optimise under the new weight distribution, forcing the various loss terms to reach lower magnitudes, thereby achieving higher solution accuracy than traditional PINN methods.

This case study clearly demonstrates that the AL-PINN framework, when solving three-dimensional transient heat conduction problems involving complex geometric configurations, not only avoids the cumbersome mesh generation process associated with traditional finite element methods but also delivers high-fidelity solutions through adaptive adjustment of physical constraint weights. Consequently, it provides effective support for the detailed thermal design of engineering structures under complex operating conditions. All computations were performed on a workstation equipped with an Intel Core i9-13900K CPU, 64 GB DDR5 RAM, and an NVIDIA RTX 3060 GPU (24 GB VRAM). The software environment consisted of Python 3. 10. 12, PyTorch 2. 1. 0 (CUDA 12. 1). All three benchmark cases were trained on the same hardware platform to ensure comparability of reported training times.

4. CONCLUSION

This study investigated transient heat conduction problems in FGMs using PINNs and AL-PINNs. By incorporating governing equations, boundary conditions, and initial conditions into the neural network loss function, the proposed framework provides a physics-informed computational approach for solving heat conduction problems with spatially varying thermal conductivity and complex geometric boundaries. This improvement is mainly due to adaptive enforcement of boundary constraints via dynamically updated Lagrange multipliers, which prevents the optimization process from being dominated by PDE residual minimization. Specifically, in the wheel hub problem, irregular hole boundaries generate large gradient discontinuities in the boundary-condition residuals. In standard PINN, these residuals are weighted equally with interior PDE residuals, causing the optimizer to prioritize bulk accuracy at the expense of boundary precision. In contrast, the Lagrange multiplier mechanism in AL-PINN specifically targets and penalizes large boundary residuals, concentrating optimization effort on geometrically challenging regions. This adaptive mechanism effectively reduces local error accumulation near complex boundaries and material-gradient regions, thereby achieving improved convergence stability and prediction accuracy. Compared with conventional PINNs that use fixed weighting coefficients, the AL-PINN framework dynamically updates the Lagrangian multipliers based on constraint residuals during training, thereby improving the balance between PDE residual minimization and boundary condition enforcement. The numerical results demonstrate that AL-PINN achieves improved convergence stability and prediction accuracy, particularly for transient heat-conduction problems involving irregular geometries and strong material-property gradients. In addition, the influence of network depth and width on prediction performance was systematically investigated, and quantitative comparisons with FEM reference solutions and analytical solutions further verified the effectiveness of the proposed framework. Nevertheless, several limitations still remain in the present study. The current work mainly focuses on benchmark numerical examples and lacks experimental validation under real engineering conditions. Furthermore, only representative transient heat-conduction problems in FGMs were considered, while more complex multi-physics coupling problems involving thermo-mechanical interactions, phase change, nonlinear radiation, or moving boundaries require further investigation. In addition, although the proposed framework reduces dependence on mesh generation, the computational cost of PINN-based methods for large-scale three-dimensional problems remains relatively high compared with conventional numerical methods. Future work will focus on experimental validation, adaptive sampling strategies, scalable parallel AL-PINN frameworks, and more realistic industrial thermal engineering applications. The proposed framework also shows potential for engineering problems involving thermal barrier coatings, aerospace thermal protection structures, and heterogeneous heat transfer systems with complex thermal boundaries. To facilitate reproducibility and independent validation, the source code, benchmark datasets, and trained model configurations will be made publicly available upon publication.

REFERENCES

[1] K. J. Gowtham, C. G. Pavithra, and B. J. Gireesha, “PINNs and Vieta-Lucas polynomial collocation simulation for heat transfer and thermal efficiency analysis in fully wetted semispherical fins with temperature-dependent thermal properties: Applications in air conditioning systems,” *Int. J. Refrig.* , vol. 181, pp. 359–369, 2026, doi: 10. 1016/j. ijrefrig. 2025. 10. 024.

[2] S. Morchio and M. Fossa, “Modelling and validation of a new hybrid scheme for predicting the performance of U-pipe borehole heat exchangers during distributed thermal response test experiments,” *Appl. Therm. Eng.* , vol. 186, p. 116514, 2021, doi: 10. 1016/j. applthermaleng. 2020. 116514.

[3] X. Wang, Z. -Y. Yin, W. Wu, and H. -H. Zhu, “Neural network-augmented differentiable finite element method for boundary value problems,” *Int. J. Mech. Sci.* , vol. 285, p. 109783, 2025, doi: 10. 1016/j. ijmecsci. 2024. 109783.

[4] K. Li, W. Jiang, and H. Li, “Isogeometric boundary element method for solving 2D multi-media heat conduction problems,” *Results Appl. Math.* , vol. 28, p. 100639, 2025, doi: 10. 1016/j. rinam. 2024. 100639.

[5] Y. Shang, H. Ban, and D. Liu, “Simultaneous identification of boundary heat flux and thermal conductivity in inverse heat conduction problems using physics-informed neural networks,” *Therm. Sci. Eng. Prog.* , vol. 65, p. 103905, 2025, doi: 10. 1016/j. tsep. 2024. 103905.

[6] A. Di Meglio, N. Massarotti, and P. Nithiarasu, “A physics-driven and machine learning-based digital twinning approach to transient thermal systems,” *Int. J. Numer. Methods Heat Fluid Flow*, vol. 34, no. 6, pp. 2229–2256, 2024, doi: 10. 1108/HFF-09-2023-0545.

[7] Y. Cui, X. Zhou, C. Fan, H. Lin, and S. Deng, “Application of physics-informed neural network-based hybrid prediction models in campus thermal environment prediction,” *Build. Environ.* , vol. 287, part B, p. 113880, 2026, doi: 10. 1016/j. buildenv. 2025. 113880.

[8] R. Zhang and L. Feng, "Application of deep learning in the prediction of heat conduction characteristics and structural optimisation of absorbing materials for solar collectors," *Microchem. J.*, vol. 221, p. 117028, 2026, doi: 10. 1016/j. microc. 2025. 117028.
[9] M. Raissi, P. Perdikaris, and G. E. Karniadakis, "Physics-informed neural networks: A deep learning framework for solving forward and inverse problems involving nonlinear partial differential equations," *J. Comput. Phys.* , vol. 378, pp. 686–707, 2019, doi: 10. 1016/j. jcp. 2018. 10. 045.
[10] G. E. Karniadakis, I. G. Kevrekidis, L. Lu, P. Perdikaris, S. Wang, and L. Yang, "Physics-informed machine learning," *Nat. Rev. Phys.* , vol. 3, no. 6, pp. 422–440, 2021, doi: 10. 1038/s42254-021-00314-5.
[11] M. Raissi, A. Yazdani, and G. E. Karniadakis, "Hidden fluid mechanics: Learning velocity and pressure fields from flow visualisations," *Science*, vol. 367, no. 6481, pp. 1026–1030, 2020, doi: 10. 1126/science. aaw1159.
[12] X. Jin, S. Cai, H. Li, and G. E. Karniadakis, "NSFnets (Navier-Stokes flow nets): Physics-informed neural networks for the incompressible Navier-Stokes equations," *J. Comput. Phys.* , vol. 426, p. 109951, 2021, doi: 10. 1016/j. jcp. 2020. 109951.
[13] L. Sun, H. Gao, S. Pan, and J. X. Wang, "Surrogate modelling for fluid flows based on physics-constrained deep learning without simulation data," *Comput. Methods Appl. Mech. Eng.* , vol. 361, p. 112732, 2020, doi: 10. 1016/j. cma. 2019. 112732.
[14] L. Yang, X. Meng, and G. E. Karniadakis, "B-PINNs: Bayesian physics-informed neural networks for forward and inverse PDE problems with noisy data," *J. Comput. Phys.* , vol. 425, p. 109913, 2021, doi: 10. 1016/j. jcp. 2020. 109913.
[15] C. Rao, H. Sun, and Y. Liu, "Physics-informed deep learning for computational elastodynamics without labelled data," *J. Eng. Mech.* , vol. 147, no. 8, p. 04021043, 2020, doi: 10. 1061/(ASCE)EM. 1943-7889. 0001947.
[16] Y. Shin, J. Darbon, and G. E. Karniadakis, "On the convergence of physics-informed neural networks for linear second-order elliptic and parabolic type PDEs," *Commun. Comput. Phys.* , vol. 28, no. 5, pp. 2042–2074, 2020, doi: 10. 4208/cicp. OA-2020-0193.
[17] L. Lu, X. Meng, Z. Mao, and G. E. Karniadakis, "DeepXDE: A deep learning library for solving differential equations," *SIAM Rev.* , vol. 63, no. 1, pp. 208–228, 2021, doi: 10. 1137/19M1274067.
[18] G. Pang, L. Lu, and G. E. Karniadakis, "fPINNs: Fractional physics-informed neural networks," *SIAM J. Sci. Comput.* , vol. 41, no. 4, pp. A2603–A2626, 2019, doi: 10. 1137/18M1204014.
[19] S. Cai, Z. Wang, S. Wang, P. Perdikaris, and G. E. Karniadakis, "Physics-informed neural networks for heat transfer problems," *J. Heat Transfer*, vol. 143, no. 6, p. 060801, 2021, doi: 10. 1115/1. 4050542.
[20] N. Zobeiry and K. D. Humfeld, "A physics-informed machine learning approach for solving heat transfer equations in advanced manufacturing and engineering applications," *Eng. Appl. Artif. Intell.*, vol. 101, p. 104232, 2021, doi: 10. 1016/j. engappai. 2021. 104232.
[21] S. A. Niaki, E. Haghighat, T. Campbell, A. Poursartip, and R. Vaziri, "Physics-informed neural networks for modelling the thermochemical curing process of composite-tool systems during manufacture," *Comput. Methods Appl. Mech. Eng.* , vol. 384, p. 113959, 2021, doi: 10. 1016/j. cma. 2021. 113959.
[22] H. Guo, X. Zhuang, P. Chen, T. Rabczuk, "Physics-informed deep learning for three-dimensional transient heat transfer analysis of functionally graded materials," Comput. Mech. , vol. 72, no. 3, pp. 537–555, 2023, doi: 10. 1007/s00466-023-02315-5.
[23] P. Das, M. A. Islam, F. R. Rijvi, M. R. Rashid, "Physics-informed operator learning integrated with analytical modeling for transient heat conduction in 2D orthotropic functionally graded materials with arbitrary gradation," Mater. Des. , vol. 259, p. 114186, 2026, doi: 10. 1016/j. matdes. 2025. 114186.
[24] A. D. Jagtap and G. E. Karniadakis, "Extended physics-informed neural networks (XPINNs): A generalised space-time domain decomposition-based deep learning framework for nonlinear partial differential equations," *Commun. Comput. Phys.* , vol. 28, no. 5, pp. 2002–2041, 2020, doi: 10. 4208/cicp. OA-2020-0164.
[25] A. D. Jagtap, E. Kharazmi, and G. E. Karniadakis, "Conservative physics-informed neural networks on discrete domains for conservation laws: Applications to forward and inverse problems," *Comput. Methods Appl. Mech. Eng.* , vol. 365, p. 113028, 2020, doi: 10. 1016/j. cma. 2020. 113028.
[26] S. Wang, Y. Teng, and P. Perdikaris, "Understanding and mitigating gradient flow pathologies in physics-informed neural networks," *J. Comput. Phys.* , vol. 443, p. 110568, 2021, doi: 10. 1016/j. jcp. 2021. 110568.
[27] S. Wang, X. Yu, and P. Perdikaris, "When and why PINNs fail to train: A neural tangent kernel perspective," *J. Comput. Phys.* , vol. 449, p. 110768, 2022, doi: 10. 1016/j. jcp. 2021. 110768.

[28] L. McClenny and U. Braga-Neto, "Self-adaptive physics-informed neural networks using a soft attention mechanism," *J. Comput. Phys.* , vol. 474, p. 111741, 2023, doi: 10. 1016/j. jcp. 2022. 111741.
[29] L. Lu, R. Pestourie, W. Yao, Z. Wang, F. Verdugo, and S. G. Johnson, "Physics-informed neural networks with hard constraints for inverse design," *SIAM J. Sci. Comput.* , vol. 43, no. 6, pp. B1105–B1132, 2021, doi: 10. 1137/20M1352327.
[30] E. Haghighat, M. Raissi, A. Moure, H. Gomez, and R. Juanes, "A physics-informed deep learning framework for inversion and surrogate modelling in solid mechanics," *Comput. Methods Appl. Mech. Eng.* , vol. 379, p. 113741, 2021, doi: 10. 1016/j. cma. 2021. 113741.
[31] Son, H. , Jang, J. W. , Han, W. J. , & Hwang, H. J. (2023). Enhanced physics-informed neural networks with augmented Lagrangian relaxation method (AL-PINNs). Neurocomputing, 548, 126424.